remote sensing

MDPI

Article

Retrieval of Carbon Dioxide Using Cross-Track Infrared Sounder (CrIS) on S-NPP

Xinxin Zhang [1,2], Ying Zhang [1,*], Lu Bai [3], Jinhua Tao [1], Liangfu Chen [1,2], Mingmin Zou [4], Zongfu Han [1] and Zhibao Wang [5]

[1] State Key Laboratory of Remote Sensing Science, Aerospace Information Research Institute, Chinese Academy of Sciences, Beijing Normal University, Beijing 100101, China; zhangxx2018@radi.ac.cn (X.Z.); taojh@radi.ac.cn (J.T.); chenlf@radi.ac.cn (L.C.); zhangxinxin18@mails.ucas.ac.cn (Z.H.)
[2] University of Chinese Academy of Sciences, Beijing 100049, China
[3] School of Computing, Ulster University, Belfast BT37 0QB, UK; l.bai@ulster.ac.uk
[4] Institute of Physical Science and Information Technology, Anhui University, Hefei 230601, China; zoumm@ahu.edu.cn
[5] School of Computer and Information Technology, Northeast Petroleum University, Daqing 163318, China; wangzhibao@nepu.edu.cn
* Correspondence: zhangying01@radi.ac.cn; Tel.: +86-13-66-13-89-24-5

Abstract: The Cross-track Infrared Sounder (CrIS) aboard the Suomi National Polar-orbiting Partnership (S-NPP) satellite is a spaceborne Fourier transform infrared spectrometer. The study aims to retrieve carbon dioxide (CO_2) information (the CO_2 profile and column-averaged dry-air mole fraction of XCO_2) from June 2018 to December 2019 based on the The National Oceanic and Atmospheric Administration (NOAA)-Unique Combined Atmospheric Processing System (NUCAPS) Cloud-Cleared Radiances (CCRs) via the CrIS. The CCRs products for the CrIS with 2223 channels have been available since 22 May 2018. Characteristics of the CO_2 weighting functions inform the choice of multiple channels that are around 15 µm in size that differ by latitude and season to maximize retrieval sensitivity to CO_2 and minimize sensitivity to other interfering atmospheric parameters. CO_2 was retrieved from these channels using an adopted nonlinear optimization algorithm. The temperature, water vapor, and ozone profiles used in the inversion process were gathered from the European Centre for Medium-Range Weather Forecasts (ECMWF) Reanalysis v5 (ERA5). Validations of CO_2 concentrations as retrieved from CrIS showed the following conclusions: (1) The relative error of the retrieved CO_2 concentrations, as compared to Civil Aircraft for the Regular Investigation of the atmosphere Based on an Instrument Container (CARIBIC) in situ aircraft measurements, was less than 0.5%, and the root mean square errors (RMSE) were less than 0.7 ppmv (with correlation coefficients of 0.56–0.86); (2) the retrieved XCO_2 from June 2018 to December 2019 correlated well with the ground-based Total Carbon Column Observing Network (TCCON) observations, and the differences were within ±0.2 ppmv. Further analysis of the temporal and spatial distribution of the retrieved CO_2 at 300 hPa demonstrated a strong seasonal variation of CO_2 in 0–60° N in the Northern Hemisphere with the maximum values in June–August and larger amplitudes of seasonal variation in the northeast of Asia and northeastern part of North America. The variations likely occurred due to larger sinks of atmospheric CO_2 that are dominated by CO_2 uptake in the summer. In the Southern Hemisphere, the CO_2 displayed high concentration anomalies in the latitudinal range of 30–60° S in September–November and December–February, which probably occurred due to the lofted smoke plumes from the strong fire seasons in South America and Southern Africa.

Keywords: Cross-track Infrared Sounder; Suomi National Polar-Orbiting Partnership; CCRs; optimization algorithm; XCO_2 and CO_2 profile

Citation: Zhang, X.; Zhang, Y.; Bai, L.; Tao, J.; Chen, L.; Zou, M.; Han, Z.; Wang, Z. Retrieval of Carbon Dioxide Using Cross-Track Infrared Sounder (CrIS) on S-NPP. *Remote Sens.* **2021**, *13*, 1163. https://doi.org/10.3390/rs13061163

Academic Editor: Michael Obland

Received: 27 January 2021
Accepted: 13 March 2021
Published: 18 March 2021

1. Introduction

Climate change is a global issue for the international community, and it is also the most serious global environmental problem that requires attention. It is time to take actions to

prevent climate change, which requires a rich understanding of the global greenhouse gas budget [1]. As one of the most important long-lived atmospheric trace gases, carbon dioxide (CO_2) is the biggest anthropogenic factor of the greenhouse effect. The concentration of atmospheric CO_2 ranged from 278 ppmv in 1750 to 300 ppmv around 0.8 million years before 1750 [2]. The World Data Centre for Greenhouse Gases (WDCGG) released the latest report on CO_2 in October of 2018, which showed that the global average CO_2 concentration reached 403.3 $\pm$ 0.1 ppmv in 2016 and that the annual mean increase in CO_2 was 3.3 ppmv from 2015 to 2016, which was greater than the previous increase from 2012 to 2013 [3]. Reasons for the rapid increase in CO_2 mainly arise from human activities which influence the exchange of CO_2 in different reservoirs. Even worse, this may lead to a ripple effect on other parts of our ecosystem, releasing more CO_2 into the air from ice and permafrost near the poles. Therefore, relatively accurate spatial and temporal information of atmospheric CO_2 contributes to a greater understanding of carbon sources and sinks, which supplies a scientific basis for policymakers to formulate emission reduction regulations [4,5].

Currently, the main methods of CO_2 detection include in situ sampling and ground and satellite-based observations. As one of the World Data Centers (WDCs), the World Data Center for Greenhouse Gases (WDCGG) can provide atmospheric parameters (e.g., CO_2 and CH_4) that are mostly monitored using ground stations [6]. Civil Aircraft for the Regular Investigation of the Atmosphere Based on an Instrument Container (CARIBIC) is a long-term atmospheric measurement program that uses a fully-automatic scientific device that is packaged in a 1.5-ton container on an airliner to measure the trace gases [7]. The Total Carbon Column Observing Network (TCCON) consists of a series of ground-based spectrometers, which can monitor atmospheric parameters, such as water vapor (H_2O), carbon monoxide (CO), methane (CH_4), and CO_2 (with an accuracy of 0.25%), among others [8]. These in situ and ground-based measurements can precisely measure the concentrations of trace gases, but they are spatially and temporally sparse in terms of the estimation of CO_2 concentrations. Spaceborne measurements with a high spatiotemporal resolution are considered to be the most effective data to capture CO_2 distributions [9–12]. So far, several spaceborne observations have been developed, including the Tropospheric Emission Spectrometer (TES) [13], the Greenhouse Gases Observing Satellite (GOSAT) [14], the Atmospheric Infrared Sounder (AIRS) [15], the Scanning Imaging Absorption Spectrometer for Atmospheric Chartography (SCIAMACHY) [16,17], the Infrared Atmospheric Sounding Interferometer (IASI) [18], the Orbiting Carbon Observatory-2 (OCO-2) [11], the Cross-track Infrared Sounder (CrIS) [19] and the Hyperspectral Infrared Atmospheric Sounder (HIRAS) [20]. The TES is a high spectral, thermal infrared sounder that was launched on the Earth Observing System Aura satellite in 2004 [21]. Kulawik et al. (2010) showed that the most sensitive altitude of TES was the middle troposphere, and the retrieved CO_2 data could contribute to quantifying CO_2 sources and sinks [21]. As the first satellite specifically designed for CO_2 monitoring, GOSAT could provide both the column-averaged CO_2 dry air mole fraction (XCO_2) and CO_2 profiles using near-infrared and thermal infrared radiances, thus promoting the research of CO_2 sources and sinks [22]. The AIRS sounder aboard the National Aeronautics and Space Administration's (NASA's) Aqua platform was the first system able to retrieve daily CO_2 measurements across the globe, with an accuracy of ~2 ppmv [23]. To achieve the global distribution (total column values) of the atmospheric trace gases, many CO_2 inversion algorithms have been applied on SCIAMACHY, and the operational CO_2 products have been produced by Institute of Environmental Physics (IUP)/ Institute of Remote Sensing (IFE) of the University of Bremen [24]. IASI, operating in the infrared band between the wavelengths of 3.6 and 15.5 μm [25], has provided information about atmospheric transport pathways and mechanisms of CO_2 transport from the surface to the upper atmosphere [26]. As one of the NASA Earth-orbiting satellites, OCO-2 has been used for studying atmospheric CO_2 concentration, which contributes to the exploration of a greater understanding of the carbon cycle [27]. CrIS, flying aboard the Suomi National Polar-Orbiting Partnership (S-NPP) and Joint Polar Satellite System (JPSS) series of satellites since 2011, can provide high-resolution temperature and moisture data

and some trace gases profiles [28]. Launched on 15 November 2017, HIRAS is an infrared sounder onboard the Feng-Yun 3D (FY-3D) satellite. With band settings similar to those of CrIS [29], HIRAS also has the ability to detect temperature, moisture, and greenhouse gases. As one of the standard sensors for calibration accuracy with other narrowband or broadband instruments, CrIS has hyperspectral characteristics and accurate radiometric and spectral identification capabilities. In our work, we performed CO_2 inversion based on CrIS, and then we compared the satellite inversion results with the CARIBIC and TCCON measurements.

Various methods have been used to retrieve concentrations of CO_2 measured by spaceborne systems. The optimal estimation approach developed by the Atmospheric CO_2 Observations from Space (ACOS) team was adopted to retrieve XCO_2 from GOSAT, and the retrieval accuracy of XCO_2 was lower than 3.5 ppmv [30,31]. The AIRS CO_2 retrieval employs an analytical method based on the partial derivative property of AIRS's 712–750 cm^{-1} region, and the retrieval results can achieve a precision of 0.43 $\pm$ 1.20 ppmv. The differential optical absorption spectroscopy (DOAS) algorithm for the retrieval of XCO_2 has been applied to SCIAMACHY sounders [32]. Kulawik et al. [21] applied the Levenberg-Marquardt (LM) algorithm to retrieve CO_2 from Tropospheric Emission Spectrometer (TES) from 40° S to 45° N with a peak sensitivity at 511 hPa. Crevoisier et al. [26] successfully inverted IASI upper tropospheric CO_2 using a neural network whose precision attained 2 ppmv with a monthly time scale. Furthermore, Crevoisier et al. [26] also pointed out the character of CO_2 emissions transported to the upper troposphere of IASI, which furnished a new vision to understand CO_2 vertical transportation in the atmosphere. The above CO_2 retrieval methods based on different satellites can reveal CO_2 distributions in the global atmosphere and capture CO_2 changes. Inspired by the updated National Aeronautics and Space Administration (NOAA)-Unique Combined Atmospheric Processing System (NUCAPS) Cloud-Cleared Radiances (CCRs) product for CrIS with a full spectral resolution, we applied a nonlinear optimization algorithm to retrieve CO_2 to evaluate the potential of CrIS in the application of CO_2 monitoring. The difference between our proposed method and other retrieval methods of CO_2 from other satellites [21,30] was the selection of channels. In this work, the selected channels were based on the characteristics of CO_2 weighting functions in different latitudes and seasons. The paper is organized as follows: Section 2 briefly introduces the sounder and its official products (CCRs and Environmental Data Records (EDR)). Section 3 provides an explanation for the retrieval method. Section 4 presents some preliminary results and comparisons. Finally, the discussions and conclusions are made in Sections 5 and 6, respectively.

2. Data

2.1. CrIS Instrument and Its Products

CrIS is mounted on the S-NPP satellite that was launched on 28 October 2011, with an inclination angle of 98.7°, a swath width of 2200 km, and a 13:30 local time for ascending node crossing [19]. CrIS provides data on 1305 channels from covers from 3.92 to 15.38 μm with unapodized spectral resolutions of 0.625, 1.25, and 2.5 cm^{-1}, respectively [33]. Considering that the central region of CO_2 infrared absorption spectra is around 4.3 μm and 15 μm, we focused on the 650–1095 cm^{-1} and 2155–2550 cm^{-1} spectral bands for CO_2 retrieval here. The Advanced Technology Microwave Sounder (ATMS) is a cross-track scanner mounted on the S-NPP [34]. CrIS, together with ATMS, have formed the Joint Polar Satellite System (JPSS) Cross-track Infrared Microwave Sounder Suite. The CrIS/ATMS system is designed to measure well-calibrated infrared and microwave radiances (called sensor data records, SDRs) for collectively retrieving atmospheric variables (Environmental Data Records (EDR)) in nonprecipitating conditions (clear, partly cloudy, and cloudy) [35].

Generally, the observations of Infrared (IR) detectors are greatly influenced by clouds. To obtain cloud-cleared radiances, the NUCAPS CCRs products for CrIS employ a cloud-clearing method to minimize cloud effects [36]. NUCAPS uses the clear sky state retrieved by ATMS to simulate a clear sky top of CrIS radiation with the field of view as a reference

and obtains the measured cloud-clear sky radiation. The method NUCAPS uses is the same as the one developed by the AIRS science team and employed in AIRS V6/V7 and the Community Long-Term Infrared Microwave Combined Atmospheric Product System (CLIMCAPS) [37–40]. The CCRs dataset was updated to version 2.0 on 22 May 2018. The difference between version 2.0 and version 1.0 is that the radiance is processed in a full spectral resolution of 0.625 cm^{-1}, and the number of channels was changed from 1305 to 2223 in version 2.0. The EDR product is from the S-NPP NOAA Unique Combined Atmospheric Processing System. It covers the inversion of multiple variables, including temperature, water vapor, ozone (O_3), CH_4, CO, CO_2, etc. Each retrieved atmospheric profile for each variable consists of 100 points from 1100 hPa to 0.016 hPa. The CO_2 products were obtained by the physical inversion method, and the details of the algorithm can be found in the theoretical basis documentation [41]. In this work, we retrieved CO_2 concentrations with CCRs from a subset of 2223 channels, and EDR CO_2 products were used to compare with our retrieved results.

2.2. Validation Data

CARIBIC is an ongoing project to detect atmospheric chemistry and composition via installing an automated laboratory on an airplane. The aircraft features a modified airfreight container with automated scientific equipment connected to air and particle inlets underneath the aircraft, which travels from Europe to many different regions across the world [7]. According to the flight height of the aircraft, the sampling times for gases range between 30 and 90 seconds with a spatial resolution of 7–21 km [42]. CARIBIC is distinguished by its ability to routinely measure a wide range of important atmospheric species [43]. The measurement precision and uncertainty for CO_2 of CARIBIC are about 0.15 and 0.20 ppmv, respectively [44]. The project has lasted for nearly 16 years, from 2004 to now, and it provides many gas components measurements, such as NO, NO_2, CH_4, and CO_2. More information about the project and system information can be found in the work of Brenninkmeijer et al. [7]. For this study, only four flights after June 2018 were available for comparison and validation. The detailed information about the four flight tracks, dates, and sampling locations can be seen in Figure 1.

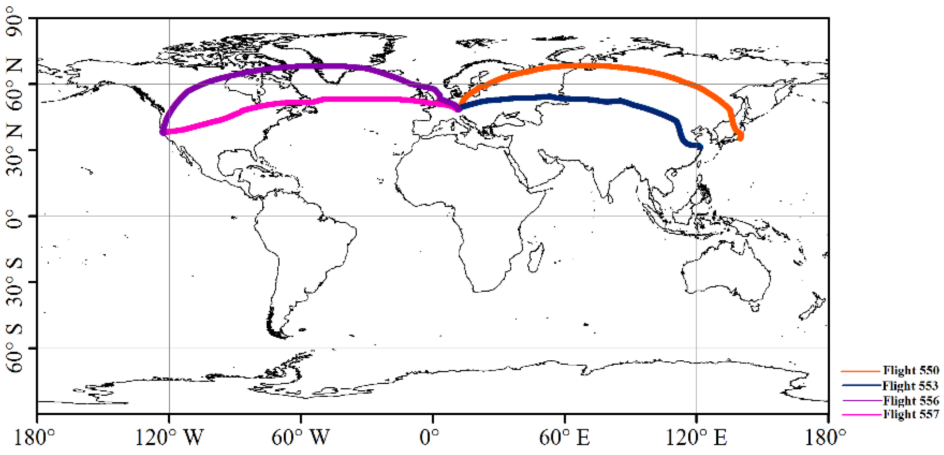

Figure 1. Civil Aircraft for the Regular Investigation of the Atmosphere Based on an Instrument Container (CARIBIC) data for four flights. Orange line is flight 550 (29 July 2018), blue line is flight 553 (31 July 2018), purple line is flight 556 (10 October 2018), pink line is flight 557 (11 October 2018).

The Total Carbon Column Observing Network (TCCON), established in 2004, is a network that can derive column abundances of many trace gases. Up to now, there are more than twenty operational TCCON sites, usually located at low altitudes, where the biosphere/ocean exchange has the most significant impact on the atmospheric concentrations [45]. More detailed information for TCCON can be found at https://tccondata.org/, accessed on 26 January 2021. The TCCON project has not only provided long time series

observation of atmospheric components but also comparative standards between ground-based observations and spaceborne measurements [8]. Considering the equator-crossing time (ascending node, 13:30) of CrIS, TCCON CO_2 measurements within two hours of the CrIS passing time were chosen to compute the daily mean values and CO_2 retrieved from CrIS within 200 km of TCCON sites. TCCON measurements from eight stations were available from 22 May 2018, when the CCRs version 2.0 started. Most of these stations are situated in mid-latitudes except Izana in the tropics. The specific information of the eight sites used for validation is listed in Table 1.

Table 1. Information for the Total Carbon Column Observing Network (TCCON) stations used for the validation.

Sites	Latitude	Longitude	Altitude (km)	Days	Start Date	End Date
Izana (Tenerife, Canary Islands, Spain) [46]	28.3	−16.48	2.37	88	5 June 2018	19 December 2019
Caltech (USA) [47]	34.14	−118.13	0.230	231	5 June 2018	31 December 2019
Edwards (USA) [48]	34.96	−117.88	0.699	218	5 June 2018	31 December 2019
Lamont (USA) [49]	36.6	−97.49	0.32	189	5 June 2018	31 December 2019
Park Falls (USA) [50]	45.94	−90.27	0.44	194	5 June 2018	7 December 2019
Garmisch (Germany) [51]	47.48	11.06	0.74	116	5 June 2018	18 October 2019
Karlsrube (Germany) [52]	49.1	8.44	0.116	87	9 July 2018	30 October 2019
East Trout Lake (Canada) [53]	54.36	−104.9900	0.5018	172	5 June 2018	30 August 2019

3. Method

3.1. The Sensitivity of CrIS Channels to CO_2

The absorption bands for CO_2 are around 4.3 μm (2325cm^{-1}) and 15 μm (666.7cm^{-1}). These two spectral bands show different sensitivities to CO_2 and other atmospheric parameters, including H_2O, temperature (T), O_3, nitrous oxide (N_2O), CO, and methane. In the longwave absorption band, channels are sensitive to H_2O and O_3, while in the shortwave band, channels are sensitive to T and CO. As stated by Crevoisier et al. [26], some rules need to be met to choose retrieval channels of CO_2, which include the sensitivity of the channels to CO_2 changes and the sensitivity of the channels to other gases and the part of the atmosphere in which the channel is sensitive to CO_2 variations. Considering the above criteria to choose the retrieval channels of CO_2, the spectral band located at 15 μm was used in this work. Nevertheless, channels near 15 μm are not only sensitive to CO_2 but also other variables, such as water vapor and ozone. The sensitivity of channels was computed through 80 globally representative Thermodynamic Initial Guess Retrieval (TIGR) [54] atmospheric profiles.

Figure 2 illustrates the brightness temperature (BT) variations corresponding to the changes of 10% CH_4, 10% CO, 10% N_2O, 10% O_3, 10% H_2O, 1 K T, and 1% CO_2. It shows that channels with a center wavenumber shorter than 700 cm^{-1} are much more sensitive to temperature, while greater than 700 cm^{-1} are more sensitive to water vapor. Generally, channels are mainly affected by temperature and water vapor in the CO_2 absorption band. Because of the huge variability of water vapor (especially in the tropical areas) and limited understanding of its tropospheric distribution, it is a challenging task to separate CO_2 signals from water vapor.

The CO_2 Jacobians were computed through 80 globally representative TIGR atmospheric profiles. These atmospheric profiles were selected from the whole profile sample set, covering the geographical range from 70° N to 70° S. These profiles samples were divided into four situations, namely, high latitude in autumn and winter (HW, 90–60° S and 60–90° N), high latitude in spring and summer (HS, 90–60° S and 60–90° N), low latitude in autumn and winter (LW, 60° S to 60° N) and low latitude in spring and summer (LS, 60° S to 60° N). Figure 3 exhibits the averaged CO_2 Jacobians of the CO_2 absorption spectral bands from 700 to 755 cm^{-1} as computed by Radiative Transfer for the Television Operational Vertical Sounder (TOVS, RTTOV) in the above four situations. We can see that the sensitivity of CO_2 peaked in the mid-upper troposphere, and the distributions of the

CO_2 Jacobians in four situations were different. The altitude of the sensitivity peak was higher for LS and lower for HW, and the amplitudes of the CO_2 Jacobians for HS and LS were larger than LW and HW, respectively. Since the temporal and spatial distribution of temperature and water vapor varied dramatically, especially in summer, and the higher the temperature, the greater the water vapor and the greater the amplitude of channel sensitivity.

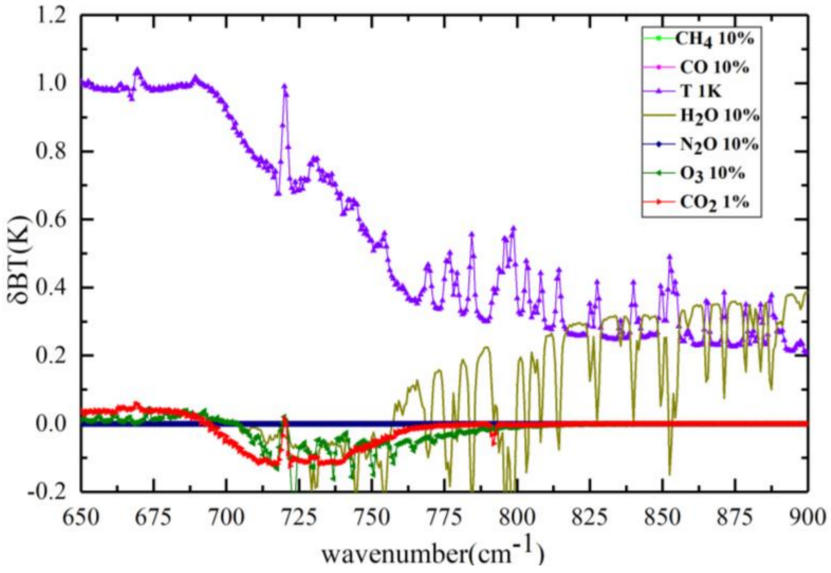

Figure 2. Sensitivities of Cross-track Infrared Sounder (CrIS) channels located in the long wave bands (650-900cm^{-1}) to variations of 10% CH_4 (green), 10% CO (pink), 10% N_2O (navy blue), 10% O_3 (olive green), 10% H_2O (deep yellow), 1 K temperature (violet), and 1% CO_2 (red).

Based on the above analysis and the redundant information of these channels near 15 μm, we selected channels that were sensitive to CO_2 but less sensitive to other perturbations. In the LS and LW situations, 28 channels were chosen for CO_2 retrieval, and the pressures of the maximum of the CO_2 Jacobians ranged from 100 to 400 hPa, while in HS and HW situation, 15 channels were selected for CO_2 retrieval, and the pressures of the maximum of CO_2 Jacobians ranged from 200 to 500 hPa. Moreover, the 28 channels in LS were completely different from those in LW, and the 15 channels in HS were completely different from those in HW. Figure 4 illustrates the selected channels near the CO_2 absorption band in different situations used to retrieve CO_2.

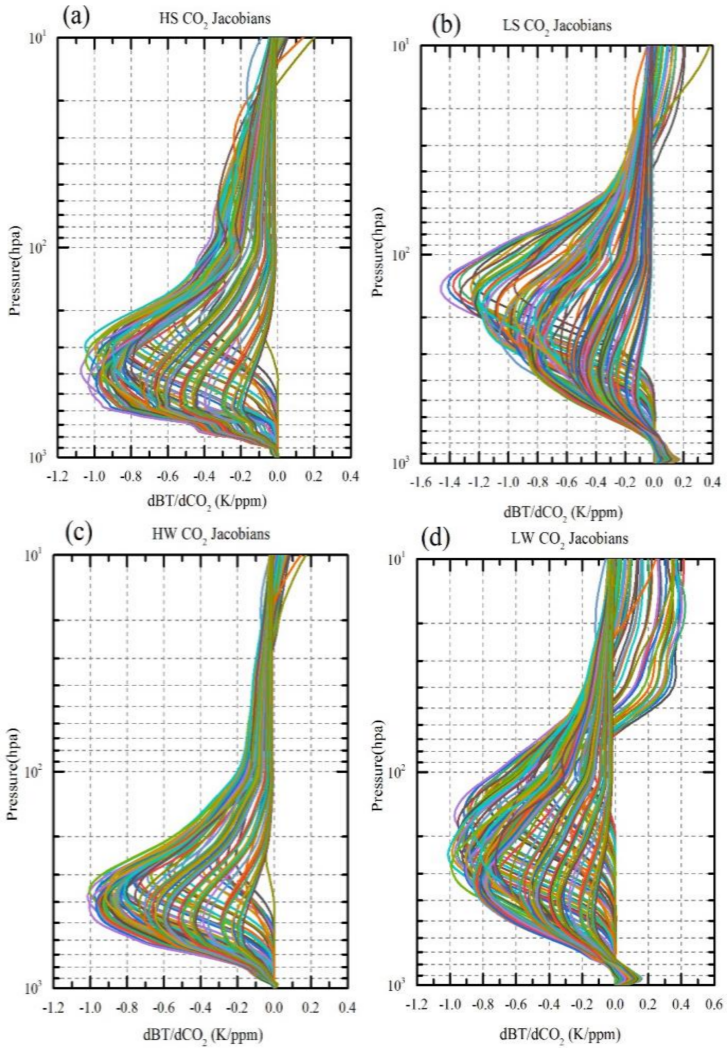

Figure 3. CO_2 Jacobians (K/ppmv) of the spectral bands from 700 to 755cm^{-1} with a spectral resolution of 0.625 cm^{-1}. (**a**) CO_2 Jacobians for high latitude in spring and summer (HS) (90–60° S and 60–90° N), (**b**) CO_2 Jacobians in low latitude in spring and summer (LS) (60° S to 60° N), (**c**) CO_2 Jacobians in high latitude in autumn and winter (HW) (90–60° S and 60–90° N), and (**d**) CO_2 Jacobians in low latitude in autumn and winter (LW) (60° S to 60° N).

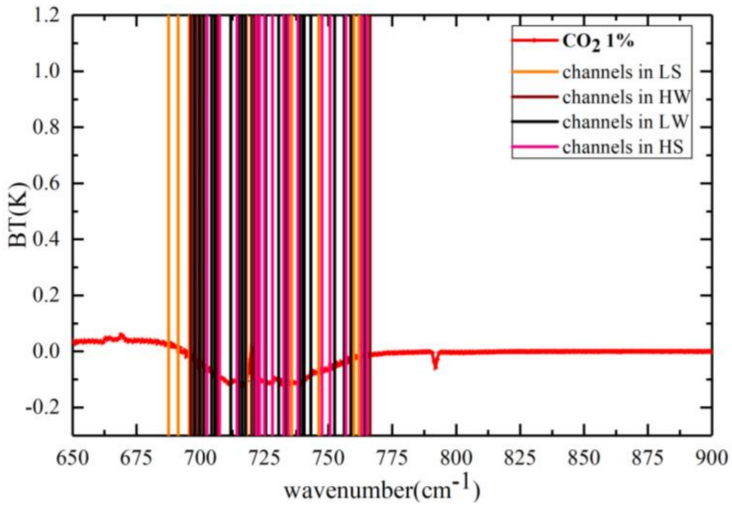

Figure 4. Selected channels used to retrieve CO_2.

3.2. Physical Retrieval Method

A physical CO_2 retrieval method aims to minimize the weighted difference between the cloud cleared radiance and the simulated radiance computed using a radiation transfer model [55]. The cost function *J(X)* can be expressed as:

$$J(X) = \min\left\{(Y^m - F(X,b))R^{-1}(Y^m - F(X,b) + (X - X_a)^T B^{-1}(X - X_a))\right\} \quad (1)$$

where Y^m is the cloud cleared radiances (observed) of selected channels m, *F(X)* is the computed radiance of the forward model, X is the full state vector which includes many elements (temperature, H_2O, O_3, and CO_2), b is the additional variables and observation metadata (scan angle, solar zenith angle, and so on) for calculating radiances, X_a is the a priori CO_2 profile, R^{-1} is the error covariance matrix of satellite observation, and B^{-1} is the inverse covariance of the a priori X_a. In this work, we chose the CCRs of CrIS as the cloud cleared radiance Y^m, and the simulated radiance *F(X)* was computed by RTTOV. The a priori state vector X_a was computed using the Empirical Orthogonal Functions (EOF) model. The radiance and atmospheric vertical profiles were expanded simultaneously by empirical orthogonal expansion, and then the statistical regression relationship between the expansion coefficients was established [56]. The atmospheric vertical profile samples were European Centre for Medium-Range Weather Forecasts (ECMWF) observation samples based on radiosonde data. The initial estimates of CO_2 used to produce a priori data were also taken from the ECMWF. About 80 samples were selected from the whole profile sample set, covering the geographical location from 70° N to 70° S. The CO_2 profiles were extracted from the experiments performed at ECMWF within the context of the Global and regional Earth-system Monitoring using Satellite and in situ data (GEMS) project [57]. All the atmospheric composition profile samples were processed into 101 layers. The atmospheric composition profiles were represented by C. The simulated radiance R based on the profiles was calculated by RTTOV, which was based on the band response function of CrIS. Thus, a statistical regression training sample set containing spatiotemporal representative atmospheric composition profiles and corresponding simulated observations was obtained. To reduce the inversion error caused by solar observation geometry, the simulated CrIS radiances were calculated at different viewing and incident zenith angles from 0° to 70° in an interval of 5° [56]. The regression coefficient matrix S under different viewing angles was generated in the calculation process [58]. The a priori CO_2 profile can be expressed as follows.

$$X_a = \overline{C} + S \times \Delta R_{obs} \quad (2)$$

where $\overline{C}$ is the mean value of the atmospheric vertical profile sample, and ΔR_{obs} is the deviation matrix between the observed radiance and the mean of the simulated radiance sample set.

The Singular Value Decomposition (SVD) algorithm proposed by Susskind [37] was applied to obtain the CO_2 profile. The simplified formula is given as follows:

$$X = X_a + UD^{-1}U^T K^T R^{-1}(Y^m - Y(X_a)) \quad (3)$$

where U is the conversion matrix, D is the eigenvalue diagonal matrix, K is the Jacobian matrix, R is the satellite observation, and X_a is the CO_2 first-guess profile.

In the retrieval method, the averaging kernels represent the proportion of information in the CO_2 retrieval profile could be expressed as follows:

$$A_k = UD^{-1}U^T K^T R^{-1} K \quad (4)$$

The atmospheric water, temperature, and ozone profiles required as inputs were gathered from European Centre for Medium-Range Weather Forecasts (ECMWF) Reanalysis v5 (ERA5) data featured by an hour time resolution and a 0.25° × 0.25° spatial resolution (https://www.ecmwf.int/, accessed on 26 January 2021). ERA5 reanalysis data assimilate

a large amount of satellite data and observation data, such as in situ observation data, which has advantages in terms of long time series recording and high spatial and temporal resolutions. The water, temperature, and ozone profiles of ERA5 have high precision. In our retrieval, the above data (e.g., CCRs, ERA5, satellite, and solar geographic information) and the first-guess profile of CO_2 were defined in the NUCAPS fast radiation transfer model to simulate radiances^{RTTOV} or BT^{RTTOV}.

4. Results

4.1. Comparison with CARIBIC

To verify the precision of the CO_2 profile inversion with CrIS, this section compares the inverted CrIS CO_2 profile with the CARIBIC observation profile. Because version 2.0 of the CCRs data was updated after 23 May 2018, we only selected the flight data after May 2018. The flight data of 10 seconds synthesis provided by the official CARIBIC website for four days (as described in Section 2.2) met our needs. The pressure for the four flights ranged from 200 to 900 hPa. To guarantee the same spatial resolutions, CARIBIC CO_2 profiles were averaged over 0.5° along the flight tracks and colocalized with a 0.5° × 0.5° average CrIS CO_2 profile. Considering the difference of distribution of CO_2 weighting function of CrIS, the comparisons were divided into mid-latitude (30° N–60° N) and high-latitude (60° N–90° N). To consider different vertical resolutions and allow meaningful comparisons with the retrieved CO_2 profiles, this paper used an averaging kernels (AK) matrix to smooth the CARIBIC observation profile [59], and the convolved CO_2 measurements were compared to the CrIS CO_2 profiles. A smoothed CARIBIC CO_2 profile can be obtained as follows:

$$\hat{X} = A_k X_c + (I - A_k) X_a \tag{5}$$

where X_c is the CARIBIC observation profile.

In Figure 5, the correlation coefficients between the CrIS CO_2 profile and smoothed CARIBIC observation profile were larger than 0.7. Table 2 shows the correlation coefficients(r), root mean square errors (RMSE), and relative errors (RD) of the CrIS CO_2 profile and smoothed CARIBIC CO_2 profile in detail. The relative error is defined as:

$$RD = \frac{|CARIBIC - Sounder|}{CARIBIC} \times 100 \tag{6}$$

The values of the RD between the CrIS CO_2 profile and CARIBIC observation profile were less than 0.5%, and the values of the RMSE were less than 0.7 ppmv. The results of Table 2 demonstrated that the correlation coefficient of CO_2 inversion in 30° N–60° N was greater than that in 60° N–90° N. This may be due to the fact that the CO_2 concentrations in high latitude are relatively smaller than that in mid-latitude and simultaneously affected by temperature and water vapor profiles. Figure 6 illustrates the correlations between CARIBIC observation profile and EDR product. The four flight CO_2 correlation coefficients between CARIBIC observation profile and EDR product were below 0.4, with correlation coefficients of flights 550, 553, 556, and 557 of −0.2, 0.35, 0.25, and 0.35, respectively.

Figure 7 shows that the mean AKs corresponding to the four flights exhibit significant overlap, and the maximal values of AK in different latitudes were obviously different. Those for the middle to high latitudes (30° N–90° N) showed that the most sensitive layer was at about 133 hPa, and for middle latitudes (30° N–60° N), the most sensitive layer was at about 200–300 hPa. The distributions of AKs in CARIBIC comparisons also corresponded to Figure 3, where temperature and water vapor greatly influenced the weighting function and the vertical sensitivity of CO_2 retrieval had geographic and seasonal variability [60]. The distribution of the CO_2 AK displayed information about the vertical resolution. Meanwhile, it also reflected the influence of the a priori profile on retrieval profile. So larger sensitivities in about 100-300 hPa suggest CO_2 in this range could be better retrieved from CrIS, while smaller sensitivity in surface shows that CrIS CO_2 profile in these altitudes would be dependent mainly on a priori.

Table 2. Comparisons between Cross-track Infrared Sounder (CrIS) CO_2 profile and Civil Aircraft for the Regular Investigation of the atmosphere Based on an Instrument Container (CARIBIC) observation profile. Average of the relative difference (RD) CARIBIC-CrIS, root mean square error (RMSE), linear correlation coefficient (r) and the number of collocated 0.5° grid cells (N).

Date	Latitude	RD (%)	RMSE (ppmv)	r	N
29 July 2018	30° N–90° N	0.19	0.49	0.78	133
	30° N–60° N	0.24	0.56	0.79	94
	60° N–90° N	0.07	0.20	0.52	39
31 July 2018	30° N–60° N	0.23	0.62	0.86	269
10 October 2018	30° N–90° N	0.08	0.41	0.70	127
	30° N–60° N	0.09	0.44	0.71	97
	60° N–90° N	0.06	0.24	0.69	30
11 October 2018	30° N–60° N	0.48	0.67	0.72	281

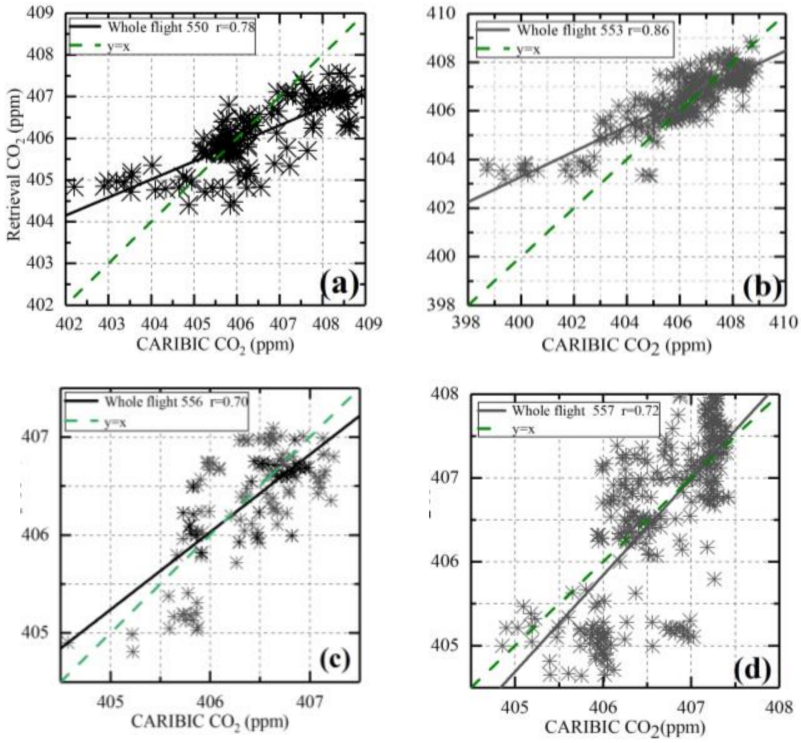

Figure 5. CO_2 comparison between smoothed CARIBIC and CrIS retrievals with the spatial resolution of 0.5° × 0.5° (**a**) flight No. 550, (**b**) flight No. 553, (**c**) flight N0. 556, (**d**) flight No. 557.

From CARIBIC's flight trajectory, we can see that the No. 556 and 557 flight paths were mostly over the ocean. Here, we divided the land and ocean according to the surface types and compared the inversion results with the smoothed values. Figure 8 depicts that the correlation of land was higher than that of ocean, while there was no significant difference between RD and RMSE. The number of samples on land and ocean was 524 and 204, respectively. It is possible to speculate that the ocean is affected by the temperature, humidity, surface reflectance, and fewer data points than the land, which results in the low correlation of the inversion results. We also found outliers of low CARIBIC values that were overestimated by CrIS retrievals over land, and conversely, high CARIBIC values that were underestimated by CrIS retrievals over ocean. In addition to the influence of temperature and humidity, it may be related to the insufficient distribution of priori profile samples in marine areas.

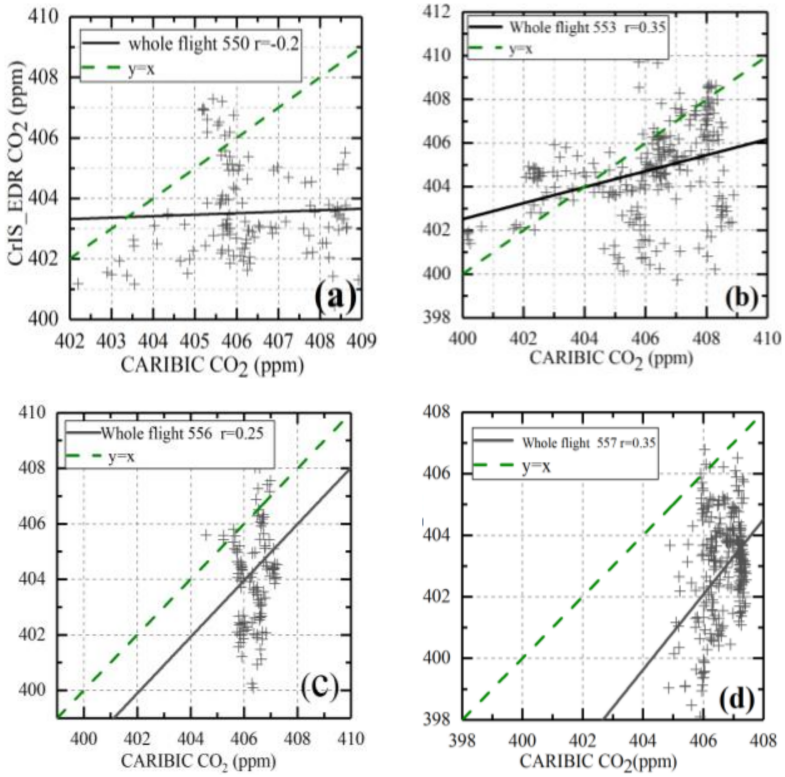

Figure 6. CO_2 comparison between smoothed CARIBIC and CrIS Environmental Data Records (EDR) with the spatial resolution of 0.5° × 0.5° (**a**) flight No. 550, (**b**) flight No. 553, (**c**) flight No. 556, (**d**) flight No. 557.

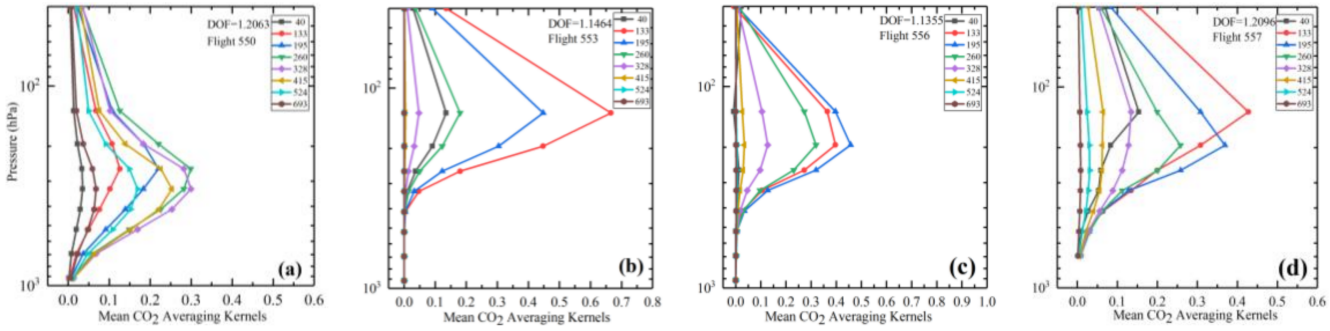

Figure 7. Mean averaging kernels of CO_2 retrievals (**a**) averaging kernels of flight No. 550, (**b**) averaging kernels of flight No. 553, (**c**) averaging kernels of flight No. 556, (**d**) averaging kernels of flight No. 557.

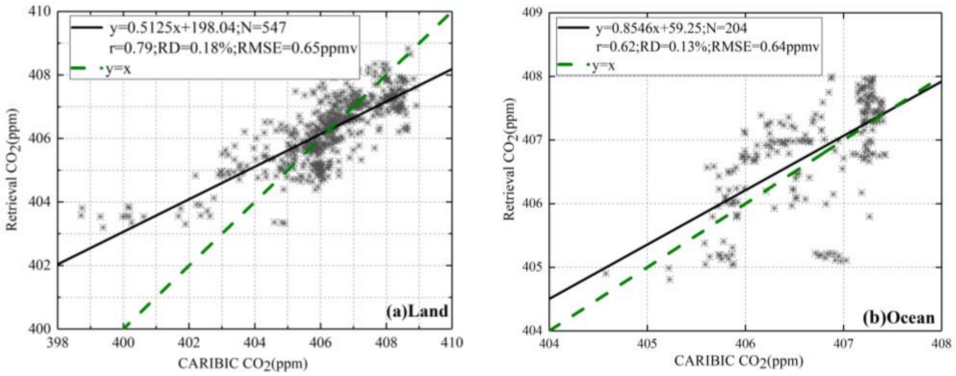

Figure 8. CO_2 comparison between smoothed CARIBIC and CrIS retrievals in (**a**) land and (**b**) ocean.

4.2. Comparison with TCCON

In this section, we provide a XCO_2 comparison between TCCON and CrIS measurements. The detailed information of TCCON sites can be seen in Table 1. To maintain sufficient data and guarantee dimensional consistency, the NUCAPS CCRs product for CrIS matched to TCCON sites was resampled at $0.5^\circ \times 0.5^\circ$ grid resolution. Rodgers and Connor [61] stated that it was unreasonable to directly compare the measurement results of different satellite sensors which had different a priori profiles and AKs. The XCO_2 of TCCON is obtained based on near-infrared inversion, which is more sensitive to CO_2 in the boundary layer of the atmosphere. Thermal infrared is more sensitive to CO_2 in the upper troposphere. The inverted AKs represent how much of the information in the inverted profile comes from the observation. Therefore, the purpose of smoothing TCCON's CO_2 profile data with the retrieved AKs was to prove the inversion accuracy of our algorithm. Following the methods of Rodgers and Connor [61] and Inoue et al. [62], the smoothing ${XCO_2}^{TCCON,smoothed}$ for TCCON weighted by the retrieval CO_2 AKs can be expressed as formula (7) [62].

$$ {XCO_2}^{TCCON,smoothed} = {XCO_2}^{a} + \sum_{j} h_j a_j (X_{TCCON,in-situ} - X_a) \quad (7) $$

$$ a_j = (h^T A_K)_j \frac{1}{h_j} (j = 1, \ldots, 100) \quad (8) $$

where j is the index of the j-th layer, h is a pressure weighting function [31], ${XCO_2}^{a}$ is the column-averaged dry air mole fractions of CO_2 for the a priori X_a, and $X_{TCCON,in-situ}$ is the retrieved CO_2 profile of TCCON. Formula (7) uses the CO_2 profile retrieved of TCCON, but TCCON only provides the a priori profile $X_{TCCON,a}$. To ensure that the obtained TCCON profile $X_{TCCON,in-situ}$ and the a prior profile $X_{TCCON,a}$ have the same shape and XCO_2 of TCCON remains unchanged, we used Formula 9 to obtain the retrieved CO_2 profile of TCCON $X_{TCCON,in-situ}$.

$$ \frac{{XCO_2}^{TCCON,a}}{{XCO_2}^{TCCON,in-situ}} = \frac{X_{TCCON,a}(i)}{X_{TCCON,in-situ}(i)} (i = 1, \ldots, 71) \quad (9) $$

$X_{TCCON,a}(i)$ (obtained from TCCON data) and $X_{TCCON,in-situ}(i)$ are the a priori and observation profile of the i-th layer. Then the obtained profile $X_{TCCON,in-situ}$ was interpolated to 100 layers according to the inversion pressure.

Figure 9 depicts the XCO_2 daily variation of the a priori, TCCON smoothing observations, and CrIS retrievals from June 2018 to 2019. Because of the missing data for the NUCAPS CCRs products for CrIS from April to July of 2019, the inversion results of TCCON stations in Figure 9 are missing in this period. Table 3 displays the average of XCO_2 comparisons between the a priori, retrieval, and smoothing TCCON results. The differences between the average of the a priori, retrieval, and smoothing TCCON results were within ± 0.2 ppmv. Compared with 2018, XCO_2 showed an increasing trend in 2019. There was little difference between the a priori retrieved and the smoothing XCO_2 in most listed TCCON stations (except East Trout Lake and Garmisch sites). The difference between the three kinds of data was within ± 0.5 ppmv for Caltech, Edwards, Izana, Karlsrube, Lamont, and Park Falls. A larger difference in East Trout Lake and Garmisch was observed in spring, autumn, and winter due to the a priori and limited observation days in different seasons. The sums of each AK column were called "areas of the AK" or the "verticality" [60,63]. The mean column AKs in different seasons for TCCON stations (as shown in Figure 10) showed that the peak sensitivity mostly occurred in summer, while the peak sensitivities appeared in East Trout Lake and Garmisch in spring and autumn, respectively. We also found that most of the maximum values of the mean column averaging kernels were greater than 0.8, but those in East Trout Lake, Karlsrube, and Garmisch were almost less than 0.6. This is related to the latitude of these stations (as shown in Table 1). Generally, the lower the

latitude is, the greater the influence of temperature and humidity profile is, and the greater the peak value of the mean column averaging kernels is.

Table 3. Average of XCO_2 comparisons between the a priori, CrIS retrieval, and smoothing TCCON results.

Scheme.	A Priori (ppmv)	CrIS Retrieved (ppmv)	Smoothing (ppmv)
Caltech (USA)	409.52	409.47	409.48
East Trout Lake (Canada)	406.05	405.97	405.82
Edwards (USA)	408	407.93	407.95
Garmisch (Germany)	406.71	406.65	406.65
Izana (Tenerife)	408.21	408.21	408.13
Karlsrube (Germany)	406.44	406.29	406.31
Lamont (USA)	408.66	408.67	408.60
Park Falls (USA)	407.29	407.17	407.23

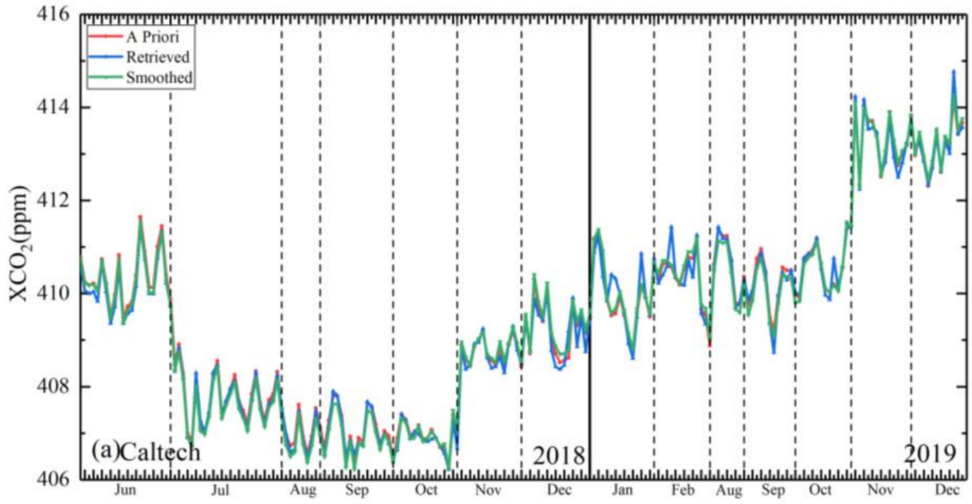

(**a**)

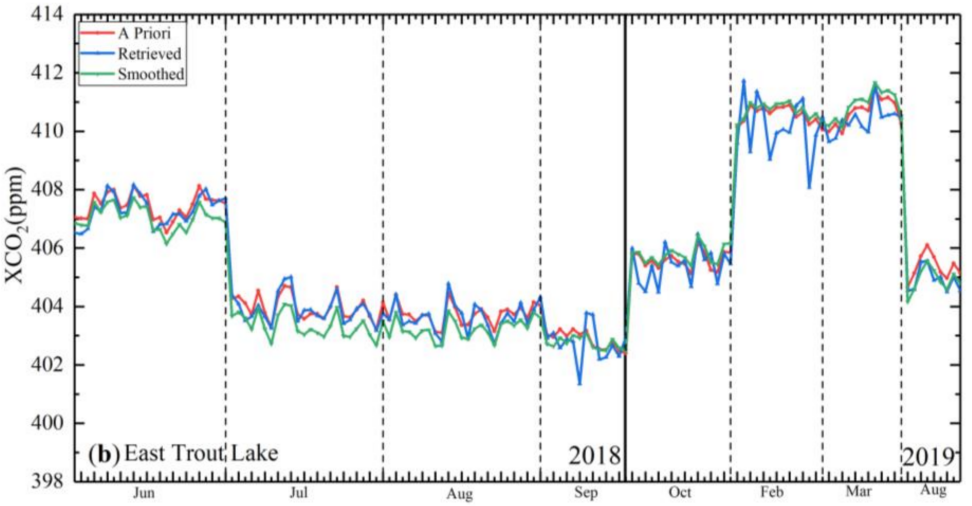

(**b**)

Figure 9. *Cont*.

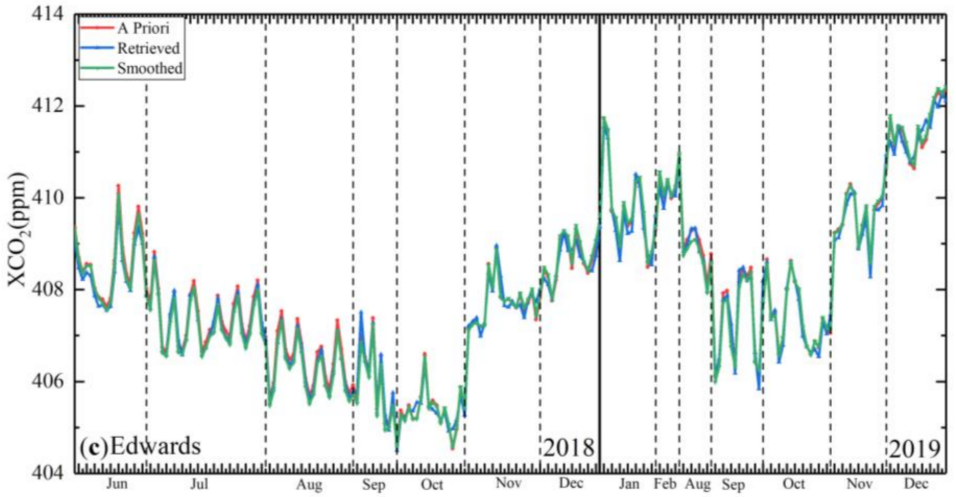

(**c**)

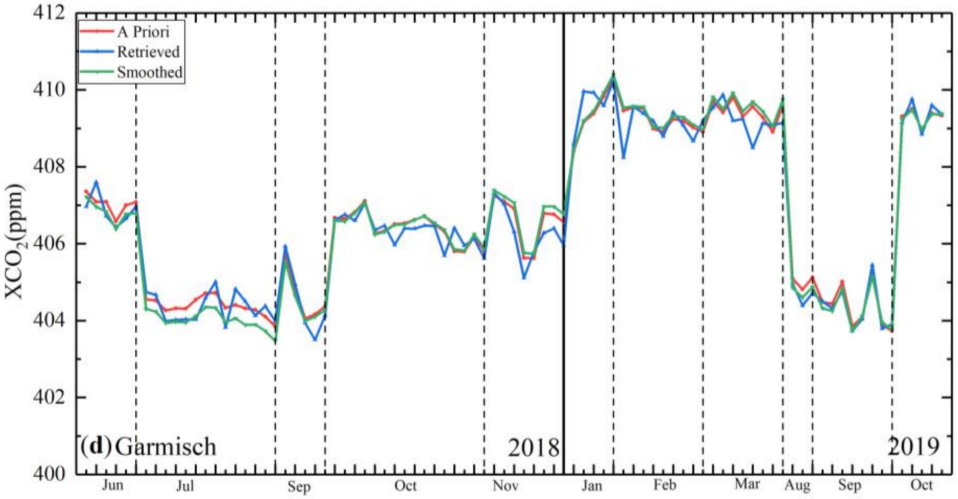

(**d**)

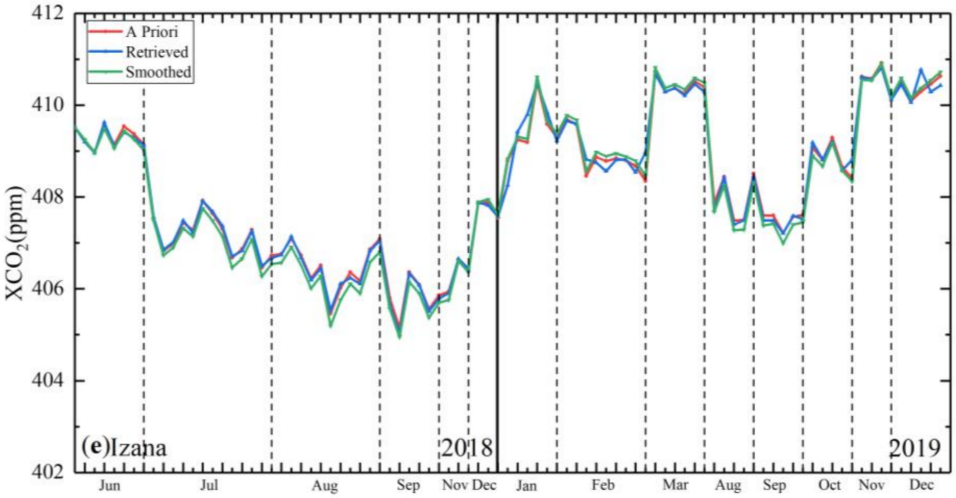

(**e**)

Figure 9. *Cont*.

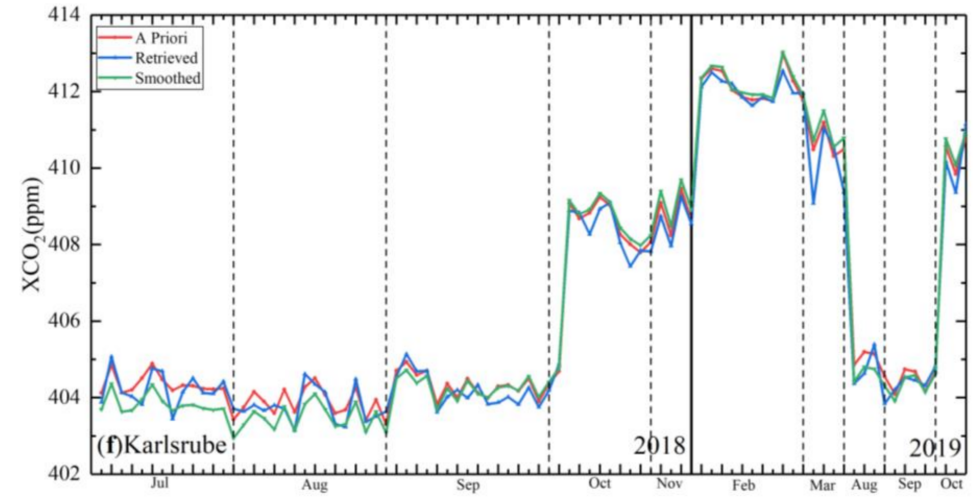

(**f**)

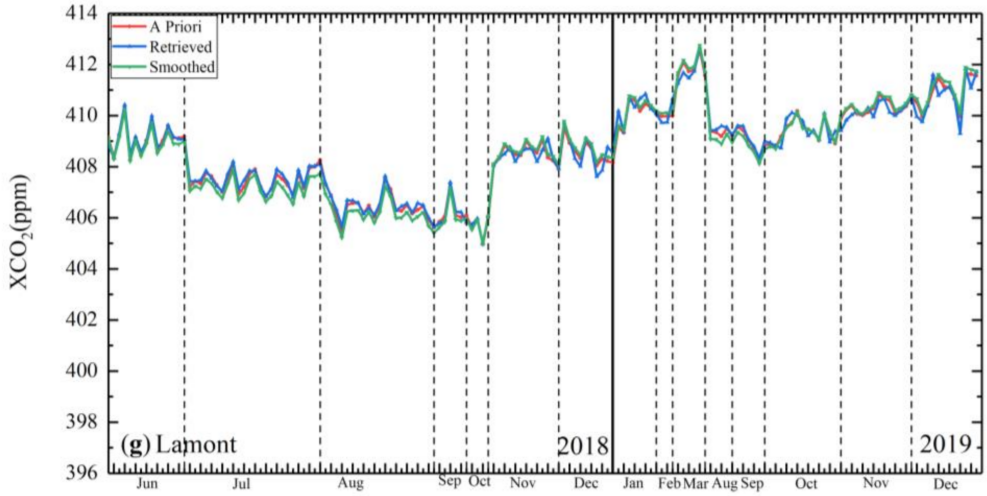

(**g**)

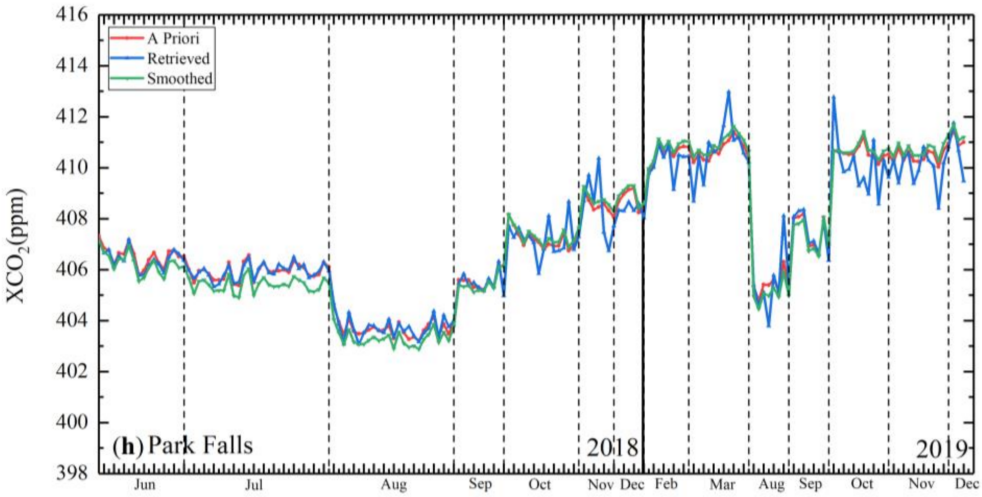

(**h**)

Figure 9. XCO_2 comparisons between a priori (red line), CrIS inversion (blue line), and smoothing Total Carbon Column Observing Network (TCCON) (green line) observation products. (**a**) Caltech, (**b**) East Trout Lake, (**c**) Edwards, (**d**) Garmisch, (**e**) Izana, (**f**) Karlsrube, (**g**) Lamont, and (**h**) Park Falls.

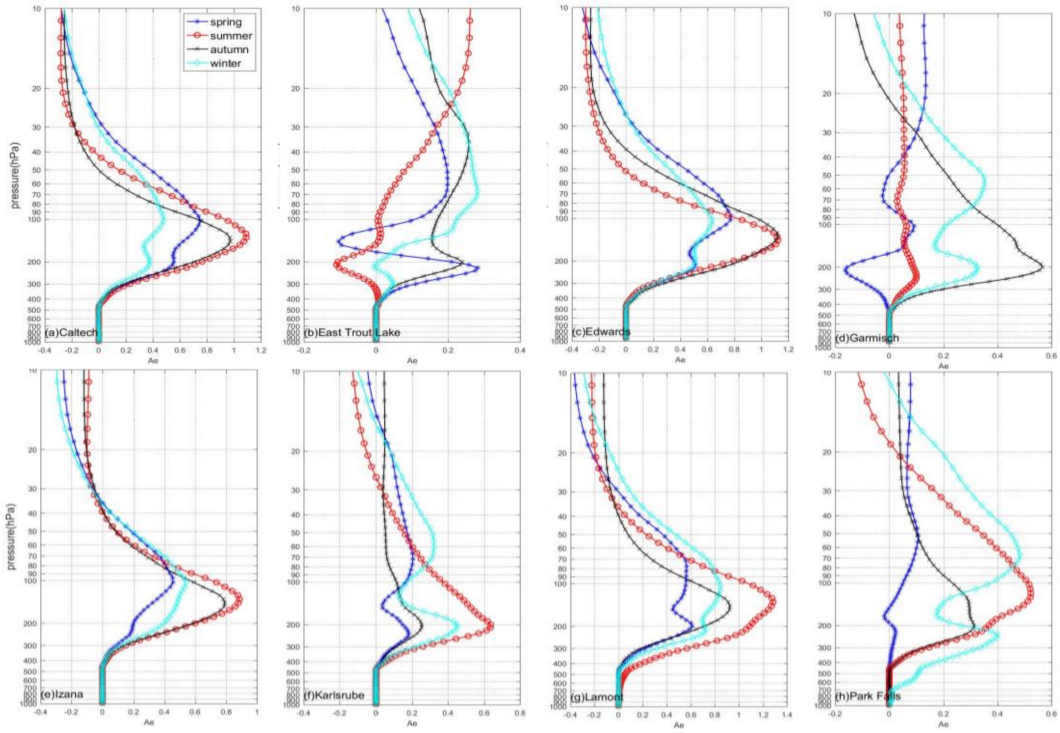

Figure 10. The mean column averaging kernels in different seasons for TCCON stations: (**a**) Caltech, (**b**) East Trout Lake, (**c**) Edwards, (**d**) Garmisch, (**e**) Izana, (**f**) Karlsrube, (**g**) Lamont, and (**h**) Park Falls. The blue, red, black, and turquoise lines represent spring, summer, autumn, and winter, respectively.

4.3. Spatial Distribution of CO_2

Based on the sensitivity of the CrIS instrument, the zonal distributions of seasonal mean CO_2 in the mid-upper troposphere at 300 hPa (60° S–60° N, 180° W–180° E) from June 2018 to May 2019 are illustrated in Figure 11, with a spatial resolution of 1° × 1°. The seasons are defined as June-July-August (JJA), September-October-November (SON), December-January-February (DJF), and March-April-May (MAM). Because of the limitations of the solar zenith angle with RTTOV, inversion values are not available in some regions.

It can be easily found that the seasonal cycle of CO_2 concentration can be clearly seen in the Northern Hemisphere. The maximum values of CO_2 retrieved from CrIS appeared in JJA with a larger CO_2 seasonal amplitude appearing in the east of Asia and the west and east of North America. A slight decrease was also observed in SON, and the minimum was reached in DJF. This trend was nearly in agreement with in situ measurements and the CO_2 retrieval from the Television Operational Vertical Sounder (TOVS) [64]. Conversely, in the Southern Hemisphere, the CO_2 variation was complicated. The CO_2 retrieval of CrIS displayed relatively high mixing ratios in the latitude zone of 30° S to 60° S in SON and DJF. This may be due to the fact that areas in the Southern Hemisphere with high CO_2 concentrations included subtropical storm paths and "convergence zone" cloud belts [65]. These cloud belts promote the convective activities of high concentrations of CO_2 and are transported to the free troposphere [23]. Moreover, the Southern Hemisphere is generally represented by a combination of biosphere and biomass burning [66]. The high CO_2 concentrations in the Southern Hemisphere could be due to lofted smoke plumes from the strong fire seasons in South America and Southern Africa.

The latitudinal gradient of CO_2 is also affected by atmospheric emission sources and the atmospheric circulation system [67]. The regions with the maximum CO_2 concentrations were mostly found in the northeast of Asia and the northeast of North America. The distributions were mainly controlled by the carbon cycle of the terrestrial biosphere [68] and the long-distance transport of greenhouse gases [69].

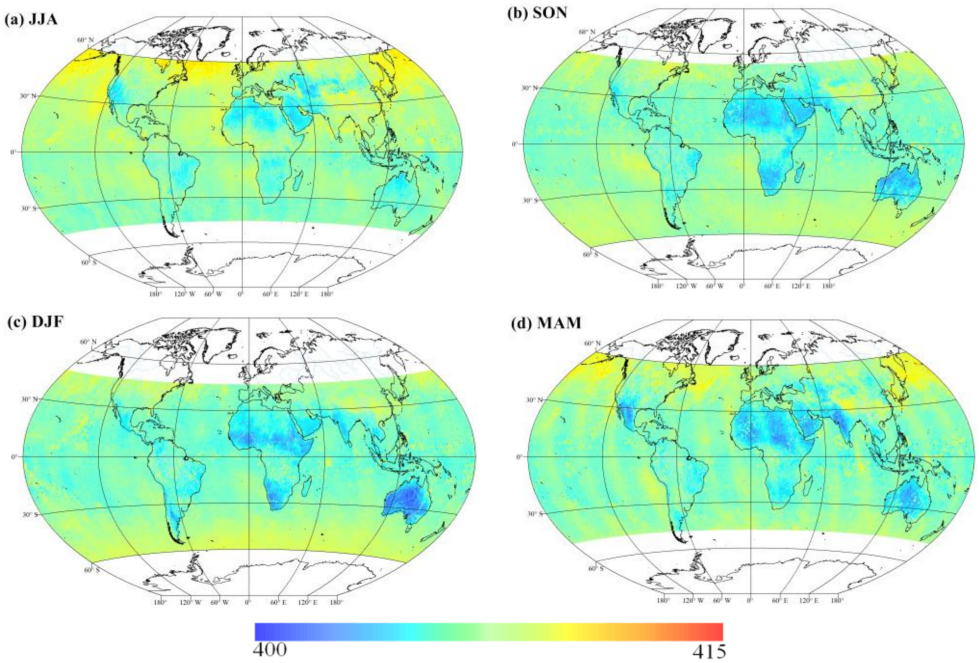

Figure 11. Seasonal CO2 at 300hPa from May 2018 to April 2019 for (**a**) June-July-August (JJM), (**b**) September-October-November (SON), (**c**) December-January-February (DJF), and (**d**) March-April-May (MAM), with 1° latitudinal resolution.

4.4. Uncertainty Analysis

In this study, the remote sensing problem of retrieving atmospheric CO_2 is ill-conditioned and has no unique solution. Therefore, not only is an optimal solution from a limited number of possible solutions needed, but the evaluation of its the accuracy is also required to analyze the various error sources and their impact on the inversion accuracy. As seen from Figure 2, the sources of errors in CO_2 inversion mainly include the temperature and water vapor profiles used for the forward model. The differences in the temperature of ERA5 in the troposphere and lower stratosphere were less than 0.2 K from 1000 hPa to 10 hPa, while the differences were greater from 10 hPa to 1 hPa and were generally ~2 K. The specific differences in the humidity of ERA5 were ~5%. In our work, according to the accuracy of the ERA5 temperature and humidity profile, the temperature profile changed by 0.2 K from 1000–10 hPa and 2 K from 10–1 hPa, and the humidity profile changed by 5% for each station (the selected TCCON stations in Section 2.2), resulting in variations in the computed CO_2 mixing ratios for June 2018 to December 2019. Table 4 shows the mean and standard deviation of variations of CO_2 induced by variations of temperature and water vapor in different seasons. The mean differences between the "modified CO_2" and the "reference CO_2" in different seasons were almost null. The standard deviations were between 1.037–2.081 ppmv, with the highest in summer and autumn and the lowest in spring. The effect of temperature and humidity changing together was almost the same as that of the temperature change.

Table 4. Means and standard deviations of variations of CO_2 induced by variations of T (1–10 hPa: 2 K; 10–1000 hPa: 0.2 K) and H_2O (5%) in different seasons.

	T	H_2O	Both Variables
Spring	0.041 1.037	0.0498 1.006	0.0372 1.042
Summer	0.0165 1.846	−0.0176 1.829	0.0155 1.854
Autumn	−0.002 2.081	−0.021 2.077	−0.006 2.080
Winter	−0.016 1.372	0.013 1.369	−0.013 1.372

5. Discussion

To prove the importance of channel selection, in this section, we carried out inversion after the retrieval channel changes for the Edwards and Izana stations in 2019 and then compared the inversion results with the inversion results in Section 4.2. The inversion channels of the Edwards station were swapped according to seasons, i.e., spring and summer used the autumn and winter channels, and autumn and winter used the spring and summer channels (as seen in Figure 12). The inversion channels of the Izana station were changed according to latitude as Izana is located in low latitude. We consequently used the channels from a high latitude area for the inversion of Izana (as seen in Figure 13). It is seen that after changing the channels that the RMSE between the inversion results and smoothing TCCON observations of Edwards increased from 0.21 to 0.52 ppmv, the average value of absolute error increased from 0.18 to 0.55 ppmv, and the maximum relative error was 2.02 ppmv. The RMSE of the inversion results of Izana increased from 0.22 to 0.53 ppmv, the average value of absolute error increased from 0.18 to 0.45 ppmv, and the maximum relative error was 1.03 ppmv. Through the above analysis, we can conclude that the inversion accuracy can be improved via the inversion of latitude and seasonal inversion channels.

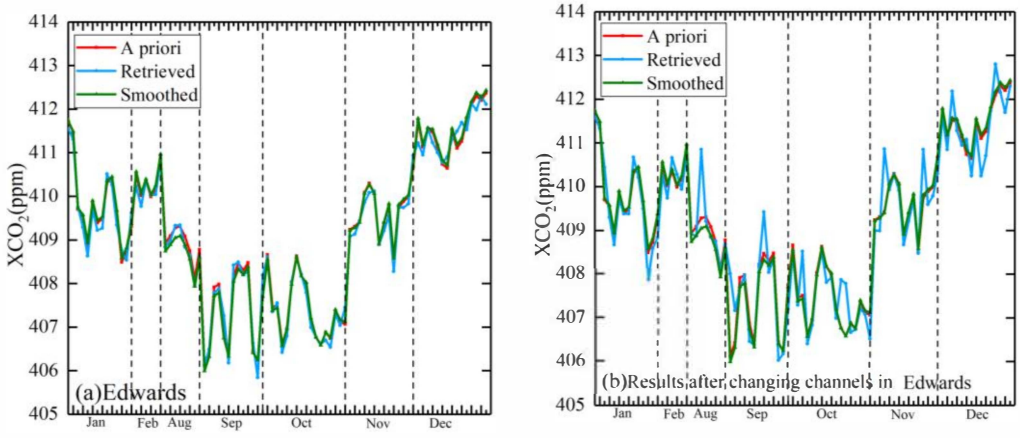

(**a**) (**b**)

Figure 12. Comparison of Edwards observations with inversion results (**a**) and inversion results using channels in opposite seasons (**b**). Red line is for a priori, blue line is for CrIS inversion, and green line is for the smoothed TCCON observation.

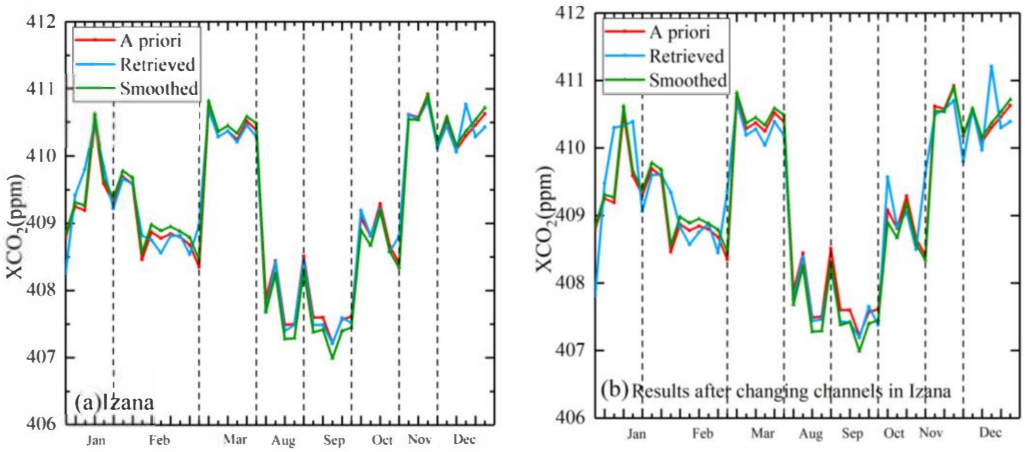

(**a**) (**b**)

Figure 13. Comparison of Izana observations with inversion results (**a**) and inversion results using channels in high latitudes (**b**). Red line is for a priori, blue line is for CrIS inversion, and green line is for the smoothed TCCON observation.

In this work, greater validation data of CARIBIC were required to prove the accuracy for CO_2 profiles in different latitudes. In later research, the biases of ERA5 parameters in different latitudes will be further investigated. We will also focus on error analysis of the algorithm and the validation of the retrieval products, and this retrieval algorithm is planned to be applied to HIRAS onboard the FY-3D satellite. Furthermore, we will quantify CO_2 sources and sinks if our retrieval results support the source of the hypothesis. We will also study the impact of transportation on the global carbon dioxide distribution [60]. It is hoped that high-quality CO_2 distribution data will lead to a better understanding of CO_2 budgets and provide the basis for reducing greenhouse gas effects.

6. Conclusions

In this paper, NUCAPS CCRs products for CrIS, with a spectral resolution of a 0.625 cm and 2223 channels (updated from 22 May 2018) with cloud effects cleared from an IR cloudy field of view, were applied to retrieve CO_2 concentrations. The operational CrIS CO_2 retrieval algorithm and some of its features were introduced in Section 3. As for this approach, a key point in selecting the retrieval channels is based on the different distributions of CO_2 Jacobians in four situations where the sensitivity reaches a peak in higher altitudes for LS and lower altitudes for HW. The peak values of the CO_2 Jacobians for HS and LS were larger than LW and HW. From the AKs, it can be concluded that the maximum sensitivity of CO_2 retrieval appeared in the mid-upper troposphere. It is worth noting that for CO_2 retrieved by CrIS with in situ measurements, the averaged correlation coefficients were 0.72 and 0.85 for CARIBIC and TCCON, with root mean square errors of 0.45 ppmv and 1.12 ppmv, respectively. Moreover, the correlation of the inversion results in 30° N–60° N was greater than that in 60° N–90° N. The relative error between the retrieval value of CrIS and the observation value of CARIBIC was less than 0.5%. The inversion values agree well with measurements from the TCCON sites. The retrieved CO_2 concentrations highlight latitudinal and seasonal variations which could be attributed to large sinks for atmospheric CO_2, where CO_2 uptake dominates during such a time. In the Southern Hemisphere, the CO_2 variation is complex. Generally, the CO_2 retrieval results based on NUCAPS CCRs products for CrIS can serve as a reference for the distribution of CO_2 in the atmosphere.

Author Contributions: Conceptualization, X.Z., Y.Z. and L.C.; methodology, Y.Z. and L.C.; software, Y.Z.; validation, X.Z.; formal analysis, X.Z. and Y.Z.; investigation, X.Z.; resources, J.T. and Y.Z.; data curation, X.Z.; writing—original draft, X.Z.; writing—review and editing, X.Z., Y.Z., L.B. and Z.H.; visualization, X.Z.; supervision, Y.Z. and L.B.; project administration, Y.Z. and L.C.; funding acquisition, Z.W., L.C., Y.Z., J.T., M.Z. All authors have read and agreed to the published version of the manuscript.

Funding: This study was supported by the National Key Research and Development Program of China (Grant No.2019YFC1509203), National Natural Science Foundation of China (41771391, 41771390), Strategic Priority Research Program of the Chinese Academy of Sciences (XDA19010403, XDA19040201), TUOHAI Special Project 2020 from Bohai Rim Energy Research Institute of Northeast Petroleum University (HBHZX202002) and the project of Excellent and Middle-Aged Scientific Research Innovation Team of Northeast Petroleum University (KYCXTD201903).

Institutional Review Board Statement: Not applicable.

Informed Consent Statement: Not applicable.

Data Availability Statement: Publicly available datasets were analyzed in this study. This data can be found here: the National Aeronautics and Space Administration (NOAA)-Unique Combined Atmospheric Processing System (NUCAPS) Cloud-Cleared Radiances (CCRs) product and Environmental Data Records (EDR) for CrIS can be found in https://www.avl.class.noaa.gov/saa/products/welcome, accessed on 26 January 2021; Civil Aircraft for the Regular Investigation of the Atmosphere Based on an Instrument Container (CARIBIC) can be found in www.caribicatmospheric.com; the European Centre for Medium-Range Weather Forecasts (ECMWF) Reanalysis v5 (ERA5) can be found in https://www.ecmwf.int/en/forecasts/datasets/reanalysis-datasets/era5, accessed on 26 January 2021; the ground-based Total Carbon Column Observing Network (TCCON) can be found in https://tccondata.org/, accessed on 26 January 2021.

Acknowledgments: We are grateful to the Joint Polar Satellite System (JPSS) and the NOAA-Unique CrIS-ATMS Processing System (NUCAPS) which provide the data for CrIS. The authors thank the IAGOS CARIBIC Community (in particular Torsten Gehrlein and Andreas Zahn) for supporting CARIBIC CO_2 data, ERA5 reanalysis data provided by ECMWF and the TCCON CO_2 data.

Conflicts of Interest: The authors declare no conflict of interest.

References

1. Umezawa, T.; Matsueda, H.; Sawa, Y.; Niwa, Y.; Machida, T.; Zhou, L. Seasonal evaluation of tropospheric CO2 over the Asia-Pacific region observed by the CONTRAIL commercial airliner measurements. *Atmos. Chem. Phys. Discuss.* **2018**, *18*, 14851–14866. [CrossRef]
2. Pearce, W.; Holmberg, K.; Hellsten, I.; Nerlich, B. Climate Change on Twitter: Topics, Communities and Conversations about the 2013 IPCC Working Group 1 Report. *PLoS ONE* **2014**, *9*, e94785. [CrossRef]
3. WMO. *Wdcgg Data Summary; Japan Meteorological Agency in Co-Operation with World Meteoro-Logical Organization*; WMO: Geneva, Switzerland, 2018.
4. Stocker, F.T.; Qin, D.; Plattner, G.-K.; Tignor, M.; Allen, S.K.; Boschung, J.; Nauels, A.; Xia, Y.; Bex, V.; Midgley, P.M. *IPCC, 2013: The Physical Science Basis. Contribution of Working Group I to the Fifth Assessment Report of the Intergovernmental Panel on Climate Change*; Cambridge University Press: Cambridge, UK, 2013; p. 1535.
5. Park, H.; Takeuchi, W.; Ichii, K. Satellite-Based Estimation of Carbon Dioxide Budget in Tropical Peatland Ecosystems. *Remote. Sens.* **2020**, *12*, 250. [CrossRef]
6. Diao, A.; Shu, J.; Song, C.; Gao, W. Global consistency check of AIRS and IASI total CO2 column concentrations using WDCGG ground-based measurements. *Front. Earth Sci.* **2017**, *11*, 1–10. [CrossRef]
7. Brenninkmeijer, C.A.M.; Crutzen, P.; Boumard, F.; Dauer, T.; Dix, B.; Ebinghaus, R.; Filippi, D.; Fischer, H.; Franke, H.; Frieβ, U.; et al. Civil Aircraft for the regular investigation of the atmosphere based on an instrumented container: The new CARIBIC system. *Atmos. Chem. Phys. Discuss.* **2007**, *7*, 4953–4976. [CrossRef]
8. Wunch, D.; Toon, G.C.; Wennberg, P.O.; Wofsy, S.C.; Stephens, B.B.; Fischer, M.L.; Uchino, O.; Abshire, J.B.; Bernath, P.F.; Biraud, S.; et al. Calibration of the Total Carbon Column Observing Network using aircraft profile data. *Atmos. Meas. Tech.* **2010**, *3*, 1351–1362. [CrossRef]
9. Houweling, S.; Hartmann, W.; Aben, I.; Schrijver, H.; Skidmore, J.; Roelofs, G.-J.; Breon, F.-M. Evidence of systematic errors in SCIAMACHY-observed CO2 due to aerosols. *Atmos. Chem. Phys. Discuss.* **2005**, *5*, 3003–3013. [CrossRef]
10. Chevallier, F.; Engelen, R.J.; Peylin, P. The contribution of AIRS data to the estimation of CO2sources and sinks. *Geophys. Res. Lett.* **2005**, *32*. [CrossRef]

11. Baker, D.F.; Bösch, H.; Doney, S.C.; O'Brien, D.; Schimel, D.S. Carbon source/sink information provided by column CO2 measurements from the Orbiting Carbon Observatory. *Atmos. Chem. Phys. Discuss.* **2010**, *10*, 4145–4165. [CrossRef]
12. Chevallier, F.; Bréon, F.-M.; Rayner, P.J. Contribution of the Orbiting Carbon Observatory to the estimation of CO2sources and sinks: Theoretical study in a variational data assimilation framework. *J. Geophys. Res. Space Phys.* **2007**, *112*. [CrossRef]
13. Nassar, R.; Logan, J.A.; Worden, H.M.; Megretskaia, I.A.; Bowman, K.W.; Osterman, G.B.; Thompson, A.M.; Tarasick, D.W.; Austin, S.; Claude, H.; et al. Validation of Tropospheric Emission Spectrometer (TES) nadir ozone profiles using ozonesonde measurements. *J. Geophys. Res. Space Phys.* **2008**, *113*. [CrossRef]
14. Lei, L.; Guan, X.; Zeng, Z.; Zhang, B.; Ru, F.; Bu, R. A comparison of atmospheric CO2 concentration GOSAT-based observations and model simulations. *Sci. China Earth Sci.* **2014**, *57*, 1393–1402. [CrossRef]
15. Crevoisier, C.; Heilliette, S.; Chédin, A.; Serrar, S.; Armante, R.; Scott, N.A. Midtropospheric CO2concentration retrieval from AIRS observations in the tropics. *Geophys. Res. Lett.* **2004**, *31*. [CrossRef]
16. Ebojie, F.; Burrows, J.P.; Gebhardt, C.; Ladstätter-Weißenmayer, A.; Von Savigny, C.; Rozanov, A.; Weber, M.; Bovensmann, H. Global tropospheric ozone variations from 2003 to 2011 as seen by SCIAMACHY. *Atmos. Chem. Phys. Discuss.* **2016**, *16*, 417–436. [CrossRef]
17. Reuter, M.; Bovensmann, H.; Buchwitz, M.; Burrows, J.P.; Connor, B.J.; Deutscher, N.M.; Griffith, D.W.T.; Heymann, J.; Keppel-Aleks, G.; Messerschmidt, J.; et al. Retrieval of atmospheric CO2with enhanced accuracy and precision from SCIAMACHY: Validation with FTS measurements and comparison with model results. *J. Geophys. Res. Space Phys.* **2011**, *116*. [CrossRef]
18. Crevoisier, C.; Nobileau, D.; Armante, R.; Crépeau, L.; Machida, T.; Sawa, Y.; Matsueda, H.; Schuck, T.; Thonat, T.; Pernin, J.; et al. The 2007–2011 evolution of tropical methane in the mid-troposphere as seen from space by MetOp-A/IASI. *Atmos. Chem. Phys. Discuss.* **2013**, *13*, 4279–4289. [CrossRef]
19. Fu, D.; Bowman, K.W.; Worden, H.M.; Natraj, V.; Worden, J.R.; Yu, S.; Veefkind, P.; Aben, I.; Landgraf, J.; Strow, L.; et al. High-resolution tropospheric carbon monoxide profiles retrieved from CrIS and TROPOMI. *Atmos. Meas. Tech.* **2016**, *9*, 2567–2579. [CrossRef]
20. Wu, C.; Qi, C.; Hu, X.; Gu, M.; Yang, T.; Xu, H.; Lee, L.; Yang, Z.; Zhang, P. FY-3D HIRAS Radiometric Calibration and Accuracy Assessment. *IEEE Trans. Geosci. Remote. Sens.* **2020**, *58*, 3965–3976. [CrossRef]
21. Kulawik, S.S.; Jones, D.B.A.; Nassar, R.; Irion, F.W.; Worden, J.R.; Bowman, K.W.; Machida, T.; Matsueda, H.; Sawa, Y.; Biraud, S.C.; et al. Characterization of Tropospheric Emission Spectrometer (TES) CO2 for carbon cycle science. *Atmos. Chem. Phys. Discuss.* **2010**, *10*, 5601–5623. [CrossRef]
22. Baker, D.F.; Doney, S.C.; Schimel, D.S. Variational data assimilation for atmospheric CO2. *Tellus B: Chem. Phys. Meteorol.* **2006**, *58*, 359–365. [CrossRef]
23. Chahine, M.T.; Chen, L.; Dimotakis, P.; Jiang, X.; Li, Q.; Olsen, E.T.; Pagano, T.; Randerson, J.; Yung, Y.L. Satellite remote sounding of mid-tropospheric CO2. *Geophys. Res. Lett.* **2008**, *35*. [CrossRef]
24. Wang, T.; Shi, J.; Jing, Y.; Xie, Y. Investigation of the consistency of atmospheric CO2 retrievals from different space-based sensors: Intercomparison and spatiotemporal analysis. *Chin. Sci. Bull.* **2013**, *58*, 4161–4170. [CrossRef]
25. Thonat, T.; Crevoisier, C.; Scott, N.A.; Chédin, A.; Schuck, T.; Armante, R.; Crépeau, L. Retrieval of tropospheric CO column from hyperspectral infrared sounders—Application to four years of Aqua/AIRS and MetOp-A/IASI. *Atmos. Meas. Tech.* **2012**, *5*, 2413–2429. [CrossRef]
26. Crevoisier, C.; Chedin, A.; Matsueda, H.; Machida, T.; Armante, R.; Scott, N.A. First year of upper tropospheric integrated content of CO2 from IASI hyperspectral infrared observations. *Atmos. Chem. Phys. Discuss.* **2009**, *9*, 4797–4810. [CrossRef]
27. Wunch, D.; Wennberg, P.O.; Osterman, G.; Fisher, B.; Naylor, B.; Roehl, C.M.; O'Dell, C.; Mandrake, L.; Viatte, C.; Kiel, M.; et al. Comparisons of the Orbiting Carbon Observatory-2 (OCO-2) XCO2 measurements with TCCON. *Atmos. Meas. Tech.* **2017**, *10*, 2209–2238. [CrossRef]
28. Lin, L.; Zou, X.; Weng, F. Combining CrIS double CO 2 bands for detecting clouds located in different layers of the atmosphere. *J. Geophys. Res. Atmos.* **2017**, *122*, 1811–1827. [CrossRef]
29. Yi, B.; Ding, S.; Bi, L. Impacts of cloud scattering properties on FY-3D HIRAS simulations. *J. Quant. Spectrosc. Radiat. Transf.* **2020**, *246*, 106902. [CrossRef]
30. O'Dell, C.W.; Connor, B.; Bösch, H.; O'Brien, D.; Frankenberg, C.; Castano, R.; Christi, M.; Eldering, D.; Fisher, B.; Gunson, M.; et al. The ACOS CO2 retrieval algorithm—Part 1: Description and validation against synthetic observations. *Atmos. Meas. Tech.* **2012**, *5*, 99–121. [CrossRef]
31. Connor, B.J.; Boesch, H.; Toon, G.; Sen, B.; Miller, C.; Crisp, D. Orbiting Carbon Observatory: Inverse method and prospective error analysis. *J. Geophys. Res. Space Phys.* **2008**, *113*. [CrossRef]
32. Reuter, M.; Buchwitz, M.; Schneising, O.; Heymann, J.; Bovensmann, H.; Burrows, J.P. A method for improved SCIAMACHY CO2 retrieval in the presence of optically thin clouds. *Atmos. Meas. Tech.* **2010**, *3*, 209–232. [CrossRef]
33. Ma, P.; Chen, L.; Wang, Z.; Zhao, S.; Li, Q.; Tao, M.; Wang, Z. Ozone Profile Retrievals from the Cross-Track Infrared Sounder. *IEEE Trans. Geosci. Remote. Sens.* **2016**, *54*, 3985–3994. [CrossRef]
34. Nalli, N.R.; Gambacorta, A.; Liu, Q.; Tan, C.; Iturbide-Sanchez, F.; Barnet, C.D.; Joseph, E.; Morris, V.R.; Oyola, M.; Smith, J.W. Validation of Atomospheric Profile Retrieval from the SNPP NOAA-Unique Combimed Atmospheric Processing System. Part 2: Ozone. *IEEE Trans. Geosci. Romote Sens.* **2018**, *56*, 598–607. [CrossRef]

35. Nalli, N.R.; Gambacorta, A.; Liu, Q.; Barnet, C.D.; Tan, C.; Iturbide-Sanchez, F.; Reale, T.; Sun, B.; Wilson, M.; Borg, L.; et al. Validation of Atmospheric Profile Retrievals From the SNPP NOAA-Unique Combined Atmospheric Processing System. Part 1: Temperature and Moisture. *IEEE Trans. Geosci. Remote. Sens.* **2017**, *56*, 180–190. [CrossRef]
36. Wang, P.; Li, J.; Li, Z.; Lim, A.H.N.; Li, J.; Schmit, T.J.; Goldberg, M.D. The Impact of Cross-track Infrared Sounder (CrIS) Cloud-Cleared Radiances on Hurricane Joaquin (2015) and Matthew (2016) Forecasts. *J. Geophys. Res. Atmos.* **2017**, *122*, 13–201. [CrossRef]
37. Susskind, J.; Barnet, C.D.; Blaisdell, J.M. Retrieval of atmospheric and surface parameters from AIRS/AMSU/HSB data in the presence of clouds. *IEEE Trans. Geosci. Remote Sens.* **2003**, *41*, 390–409. [CrossRef]
38. Susskind, J.; Blaisdell, J.M.; Iredell, L.; Keita, F. Improved Temperature Sounding and Quality Control Methodology Using AIRS/AMSU Data: The AIRS Science Team Version 5 Retrieval Algorithm. *IEEE Trans. Geosci. Remote. Sens.* **2011**, *49*, 883–907. [CrossRef]
39. Smith, N.; Barnet, C.D. Uncertainty Characterization and Propagation in the Community Long-Term Infrared Microwave Combined Atmospheric Product System (CLIMCAPS). *Remote. Sens.* **2019**, *11*, 1227. [CrossRef]
40. Smith, N.; Barnet, C.D. CLIMCAPS observing capability for temperature, moisture, and trace gases from AIRS/AMSU and CrIS/ATMS. *Atmos. Meas. Tech.* **2020**, *13*, 4437–4459. [CrossRef]
41. Gambacorta, N.R.N.A.; Barnet, C.D.; Tan, C.; Iturbide-Sanchez, F.; Zhang, K.; The NOAA Unique Combined Atmospheric Processing System (NUCAPS) Algorithm Theoretical Basis Document. NOAA, Ed.; 2017. Available online: https://www.star.nesdis.noaa.gov/jpss/documents/ATBD/ATBD_NUCAPS_v2.0.pdf (accessed on 14 August 2017).
42. Schuck, T.J.; Brenninkmeijer, C.A.M.; Baker, A.K.; Šlemr, F.; Von Velthoven, P.F.J.; Zahn, A. Greenhouse gas relationships in the Indian summer monsoon plume measured by the CARIBIC passenger aircraft. *Atmos. Chem. Phys. Discuss.* **2010**, *10*, 3965–3984. [CrossRef]
43. Baker, A.K.; Slemr, F.; Brenninkmeijer, C.A.M. Analysis of non-methane hydrocarbons in air samples collected aboard the CARIBIC passenger aircraft. *Atmos. Meas. Tech.* **2010**, *3*, 311–321. [CrossRef]
44. Assonov, S.S.; Brenninkmeijer, C.A.M.; Schuck, T.J.; Taylor, P. Analysis of 13C and 18O isotope data of CO2 in CARIBIC aircraft samples as tracers of upper troposphere/lower stratosphere mixing and the global carbon cycle. *Atmos. Chem. Phys. Discuss.* **2010**, *10*, 8575–8599. [CrossRef]
45. Messerschmidt, J.; Geibel, M.C.; Blumenstock, T.; Chen, H.; Deutscher, N.M.; Engel, A.; Feist, D.G.; Gerbig, C.; Gisi, M.; Hase, F.; et al. Calibration of TCCON column-averaged CO2: The first aircraft campaign over European TCCON sites. *Atmos. Chem. Phys. Discuss.* **2011**, *11*, 10765–10777. [CrossRef]
46. Blumenstock, T.; Hase, F.; Schneider, M.; García, O.E.; Sepúlveda, E. TCCON Data from Izana (ES), Release GGG2014.R1 (Version R1), TCCON Data Archive, Hosted by CaltechDATA. 2007. Available online: https://doi.org/10.14291/TCCON.GGG2014.IZANA01.R1 (accessed on 20 January 2020).
47. Wennberg, P.O.; Wunch, D.; Roehl, C.M.; Blavier, J.-F.; Toon, G.C.; Allen, N.T. TCCON Data from Caltech (US), Release GGG2014.R1 (Version GGG2014.R1), TCCON Data Archive, Hosted by CaltechDATA. 2015. Available online: https://doi.org/10.14291/TCCON.GGG2014.PASADENA01.R1/1182415 (accessed on 20 January 2020).
48. Iraci, L.T.; Podolske, J.R.; Hillyard, P.W.; Roehl, C.; Wennberg, P.O.; Blavier, J.-F.; Landeros, J.; Allen, N.; Wunch, D.; Zavaleta, J.; et al. TCCON Data from Edwards (US), Release GGG2014.R1 (Version GGG2014.R1), TCCON Data Archive, Hosted by CaltechDATA. 2016. Available online: https://doi.org/10.14291/TCCON.GGG2014.EDWARDS01.R1/1255068 (accessed on 20 January 2020).
49. Wennberg, P.O.; Wunch, D.; Roehl, C.M.; Blavier, J.-F.; Toon, G.C.; Allen, N.T. TCCON Data from Lamont (US), Release GGG2014.R1 (Version GGG2014.R1), TCCON Data Archive, Hosted by CaltechDATA. 2016. Available online: https://doi.org/10.14291/TCCON.GGG2014.LAMONT01.R1/1255070 (accessed on 20 January 2020).
50. Wennberg, P.O.; Roehl, C.M.; Wunch, D.; Toon, G.C.; Blavier, J.-F.; Washenfelder, R.; Keppel-Aleks, G.; Allen, N.T.; Ayers, J. TCCON data from Park Falls (US), Release GGG2014.R1 (Version GGG2014.R1), TCCON Data Archive, Hosted by CaltechDATA. 2017. Available online: https://doi.org/10.14291/TCCON.GGG2014.PARKFALLS01.R1 (accessed on 20 January 2020).
51. Sussmann, R.; Rettinger, M. TCCON Data from Garmisch (DE), Release GGG2014.R2 (Version R2), TCCON Data Archive, Hosted by CaltechDATA. 2018. Available online: https://doi.org/10.14291/TCCON.GGG2014.GARMISCH01.R2 (accessed on 20 January 2020).
52. Hase, F.; Blumenstock, T.; Dohe, S.; Groß, J.; Kiel, M. TCCON Data from Karlsruhe (DE), Release GGG2014.R1 (Version GGG2014.R1), TCCON Data Archive, Hosted by CaltechDATA. 2015. Available online: https://doi.org/10.14291/TCCON.GGG2014.KARLSRUHE01.R1/1182416 (accessed on 20 January 2020).
53. Wunch, D.; Mendonca, J.; Colebatch, O.; Allen, N.T.; Blavier, J.-F.; Roche, S.; Hedelius, J.; Neufeld, G.; Springett, S.; Worthy, D.; et al. TCCON Data from East Trout Lake, SK (CA), Release GGG2014.R1 (Version R1), TCCON Data Archive, Hosted by CaltechDATA. 2018. Available online: https://doi.org/10.14291/TCCON.GGG2014.EASTTROUTLAKE01.R1 (accessed on 20 January 2020).
54. Chevallier, F.; Chéruy, F.; Scott, N.A.; Chédin, A. A Neural Network Approach for a Fast and Accurate Computation of a Longwave Radiative Budget. *J. Appl. Meteorol.* **1998**, *37*, 1385–1397. [CrossRef]
55. Strow, L.; Hannon, S.; De Souza-Machado, S.; Motteler, H.; Tobin, D. An overview of the AIRS radiative transfer model. *IEEE Trans. Geosci. Remote. Sens.* **2003**, *41*, 303–313. [CrossRef]

56. Zhang, Y.; Xiong, X.; Tao, J.; Yu, C.; Zou, M.; Su, L.; Chen, L. Methane retrieval from Atmospheric Infrared Sounder using EOF-based regression algorithm and its validation. *Chin. Sci. Bull.* **2014**, *59*, 1508–1518. [CrossRef]
57. Marco, M. The Generation of RTTOV Regression Coefficients for IASI and Airs Using a New Profile Training Set and a New Line-by-Line Database; ECMWF Technical Memoranda. ECMWF: Reading, UK, 2008; Available online: https://www.ecmwf.int/node/11040 (accessed on 26 January 2021).
58. Zhang, Y.; Tao, J.H.; Su, L.; Yu, C.; Fan, M. Retrieval of methane profiles from spaceborne hyperspectral infrared observations. *J. Remote Sens.* **2012**, *16*, 232–247.
59. Xiong, X.; Han, Y.; Liu, Q.; Weng, F. Comparison of Atmospheric Methane Retrievals From AIRS and IASI. *IEEE J. Sel. Top. Appl. Earth Obs. Remote. Sens.* **2016**, *9*, 3297–3303. [CrossRef]
60. Xiong, X.; Barnet, C.; Maddy, E.; Sweeney, C.; Liu, X.; Zhou, L.; Goldberg, M. Characterization and validation of methane products from the Atmospheric Infrared Sounder (AIRS). *J. Geophys. Res. Space Phys.* **2008**, *113*. [CrossRef]
61. Rodgers, C.D.; Connor, B.J. Intercomparison of remote sounding instruments. *J. Geophys. Res. Space Phys.* **2003**, *108*. [CrossRef]
62. Inoue, M.; Morino, I.; Uchino, O.; Miyamoto, Y.; Yoshida, Y.; Yokota, T.; Machida, T.; Sawa, Y.; Matsueda, H.; Sweeney, C.; et al. Validation of XCO2 derived from SWIR spectra of GOSAT TANSO-FTS with aircraft measurement data. *Atmos. Chem. Phys. Discuss.* **2013**, *13*, 9771–9788. [CrossRef]
63. McMillan, W.W.; Barnet, C.; Strow, L.; Chahine, M.T.; McCourt, M.L.; Warner, J.X.; Novelli, P.C.; Korontzi, S.; Maddy, E.S.; Datta, S. Daily global maps of carbon monoxide from NASA's Atmospheric Infrared Sounder. *Geophys. Res. Lett.* **2005**, *32*, L11801. [CrossRef]
64. Ch'edin, A.; Serrar, S.; Scott, N.A.; Crevoisier, C.; Armante, R. First global measurement of mid-tropospheric CO2 from NOAA polar satellites: Tropical zone. *J. Geophys. Res.* **2003**, *108*, 4581. [CrossRef]
65. Hoskins, B.J.; Hodges, K.I. A New Perspective on Southern Hemisphere Storm Tracks. *J. Clim.* **2005**, *18*, 4108–4129. [CrossRef]
66. Deutscher, N.M.; Sherlock, V.; Fletcher, S.E.M.; Griffith, D.W.T.; Notholt, J.; Macatangay, R.; Connor, B.J.; Robinson, J.; Shiona, H.; Velazco, V.A.; et al. Drivers of column-average CO2 variability at Southern Hemispheric Total Carbon Column Observing Network sites. *Atmos. Chem. Phys. Discuss.* **2014**, *14*, 9883–9901. [CrossRef]
67. Stohl, A.; Eckhardt, S.; Forster, C.; James, P.; Spichtinger, N. On the pathways and timescales of intercontinental air pollution transport. *J. Geophys. Res. Space Phys.* **2002**, *107*, 1–17. [CrossRef]
68. Shim, C.; Lee, J.; Wang, Y. Effect of continental sources and sinks on the seasonal and latitudinal gradient of atmospheric carbon dioxide over East Asia. *Atmos. Environ.* **2013**, *79*, 853–860. [CrossRef]
69. Liang, Q.; Jaeglé, L.; Jaffe, D.A.; Weiss-Penzias, P.; Heckman, A.; Snow, J.A. Long-range transport of Asian pollution to the northeast Pacific: Seasonal variations and transport pathways of carbon monoxide. *J. Geophys. Res. Space Phys.* **2004**, *109*, 1–18. [CrossRef]